Analyst

ROYAL SOCIETY OF CHEMISTRY

PAPER

View Article Online
View Journal | View Issue



Cite this: *Analyst*, 2021, **146**, 4557

# A label-free electrochemical platform based on a thionine functionalized magnetic Fe–N–C electrocatalyst for the detection of microRNA-21†

Xiangyu Ma,[a] Kun Qian,[a] Onome Ejeromedoghene,[a] Martha Kandawa-Schulz,[b] Wei Song[b] and Yihong Wang *[a]

Taking a composite of a nanomaterial and a signal molecule as a substrate material can provide a label-free electrochemical platform. Besides, the nanomaterial with a high catalytic activity towards the signal molecule can improve the sensitivity of the platform. Herein, a thionine functionalized Fe–N–C nanocomposite was employed as the substrate. Firstly, the electrocatalytic activity of Fe–N–C towards the electroreduction of thionine was explored. Then, an immobilization-free and label-free electrochemical platform for the determination of microRNA-21 based on Fe–N–C–thionine/$Fe_3O_4$@AuNPs was constructed. A magnetic glassy carbon electrode (MGCE) was used to keep the magnetic Fe–N–C–thionine/$Fe_3O_4$@AuNPs modified onto the surface of the MGCE. Fe–N–C and $Fe_3O_4$ nanoparticles can co-catalyze the electroreduction of thionine and a strong electrochemical reduction signal of thionine could be realized in the differential pulse voltammetry (DPV) test. Also, a catalytic hairpin assembly (CHA) reaction was utilized to enhance the sensitivity of the developed electrochemical biosensor. Besides, the developed biosensor shows excellent specificity and reproducibility in the test of human serum samples, indicating its wide application prospects in the early-stage diagnosis of tumors.

Received 11th March 2021,
Accepted 27th May 2021

DOI: 10.1039/d1an00430a

rsc.li/analyst



## 1 Introduction

Recently, a variety of electrochemical biosensors have been developed for disease diagnosis.[1,2] As an indispensable part of the electrochemical biosensor, a substrate material with excellent properties can improve the sensitivity of the biosensor.[3] Typically, some natural biological enzymes such as peroxidase, superoxide dismutase, glucose oxidase, catalase and alkaline phosphatase[4–6] were immobilized onto the working electrode to recognize the target and generate electrochemical signals. However, these biological enzymes are usually easily degraded by proteolysis, and their catalytic activities are unstable because their natural structure can be readily affected by the environment. Besides, it is time-consuming and expensive to prepare, purify and store the enzymes. Hence, highly efficient non-enzymatic electrocatalysts are very desirable. Fortunately, with the development of nanotechnology, electrochemical biosensors constructed with the assistance of nanomaterials can achieve the advantages of simplicity, low cost and high sensitivity. Various nanomaterials such as metallic,[7,8] nonmetallic[9,10] and hybrid nanocomposites[11] have been employed to construct electrochemical biosensors.

Metal–organic frameworks (MOFs), a class of promising hybrid porous nanomaterials, have gained great interest in various fields such as gas storage,[12] catalysis,[13] drug delivery[14,15] and sensors[16–18] because of their excellent advantages of ordered porosity, large surface area and designable pore sizes.[19–23] Recently, MOFs have been used as nanozymes in the detection of glucose,[24] $H_2O_2$ [18] and phenol[25] due to their peroxidase-like, oxidase-like, hydrolase-like and superoxide dismutase-like activities.[26] Furthermore, MOFs have been recognized as a container of the electrochemical signal molecule to enrich the signal molecules onto the electrode. For example, Sun *et al.*[27] developed a sandwich electrochemical biosensor for the determination of tumor-derived exosomes, in which Zr-MOF nanoparticles were incubated with methylene blue (MB) and a MB@Zr-MOFs composite was formed as a strong electrochemical signal donor.

However, the poor conductivity of the MOF limits its application in electrochemical biosensors. Although some conductive MOFs have been developed, *e.g.* $Ni_3(HITP)_2$ [28] and $Cu_3(TABTO)_2$-MOF,[29] their ligands are not easily available and

[a]*School of Chemistry and Chemical Engineering, Southeast University, Nanjing 211189, PR China. E-mail: yihongwang@seu.edu.cn; Tel: (+86) 15996315308*
[b]*Department of Chemistry and Biochemistry, University of Namibia, Windhoek, Namibia*

†Electronic supplementary information (ESI) available. See DOI: 10.1039/d1an00430a

the lack of some functional groups has stalled their wide applicability. Moreover, the conductivity of most pristine MOFs could be improved after pyrolyzing.[30] For example, Sun *et al.*[31] utilized a pyrolyzed Co/Zn bimetallic organic framework to electrochemically detect formaldehyde. A variety of MOFs were pyrolyzed to enhance their catalytic activity, such as Ni-MOF,[32] Cu-MOF,[33] Fe-MOF[34] and Co-MOF.[35] Among these pyrolyzed MOFs, structures containing Fe–N–C were widely used in the biosensors for their high catalytic activity and the discovery of a special structure Fe–N in the natural enzyme.[36]

Therefore, a Fe–N–C nanomaterial should be a good candidate for the substrate material. However, a Fe–N–C nanomaterial cannot be widely used in the electrochemical biosensors only by the activity of nanozyme. Thionine, a phenothiazine dye, has been widely used as an electroactive molecule for its stability, fast electron transfer ability and good electrochemical reversibility. The electrocatalytic activity of Fe–N–C towards thionine has not been reported. Interestingly, we found that Fe–N–C possesses excellent electrocatalytic activity towards thionine. Furthermore, MOF-derived magnetic Fe–N–C could adsorb thionine as well, which can be employed to construct a label-free electrochemical platform.

MicroRNA-21 (miRNA-21), a single-strand RNA, plays an essential role in the proliferation, invasion and angiogenesis of tumors.[37,38] Nevertheless, abnormal expression of miRNA-21 has been demonstrated in many diseases including lung cancer, breast cancer and diabetes.[39]

Here, we designed an electrochemical biosensor based on a Thi functionalized Fe–N–C nanocomposite for the detection of miRNA-21, and the principle is shown in Scheme 1. Firstly, Fe–N–C was incubated with thionine to form the composite of Fe–N–C–Thi. Fe–N–C and $Fe_3O_4$ could co-catalyze the electroreduction of thionine. Therefore, a strong electrochemical signal could be obtained as a control. $Fe_3O_4$@AuNPs were used to immobilize the sulfhydryl functionalized hairpin probe H1 through an Au–S bond. Both the Fe–N–C–thionine and $Fe_3O_4$@AuNPs could be immobilized on the surface of the MGCE using an external magnet. To further enhance the sensitivity of the sensor, a catalytic hairpin assembly reaction (CHA) was employed. CHA could be triggered with the presence of the target, and $SiO_2$ with poor conductivity linked with hairpin probe 2 (H2) could be immobilized on the working electrode. Consequently, the electrochemical signal will decrease related to the concentration of the target miRNA-21. The present study offers an alternative signal amplification strategy for electrochemical biosensors. The Fe–N–C–Thi modified electrode provides a strong electrochemical signal, as a blank current, and can detect other biomarkers universally. This indicates that the developed sensing strategy may provide a new pathway in bioanalysis.

## 2 Experimental

### 2.1 Chemicals and reagents

Zinc nitrate, 2-methylimidazole, 3-(triethoxysilyl)propylsuccinic anhydride (TESPSA) and ferric chloride were provided by Sinopharm Chemical Reagent Co., Ltd. 1-Ethyl-3-(3-dimethyl

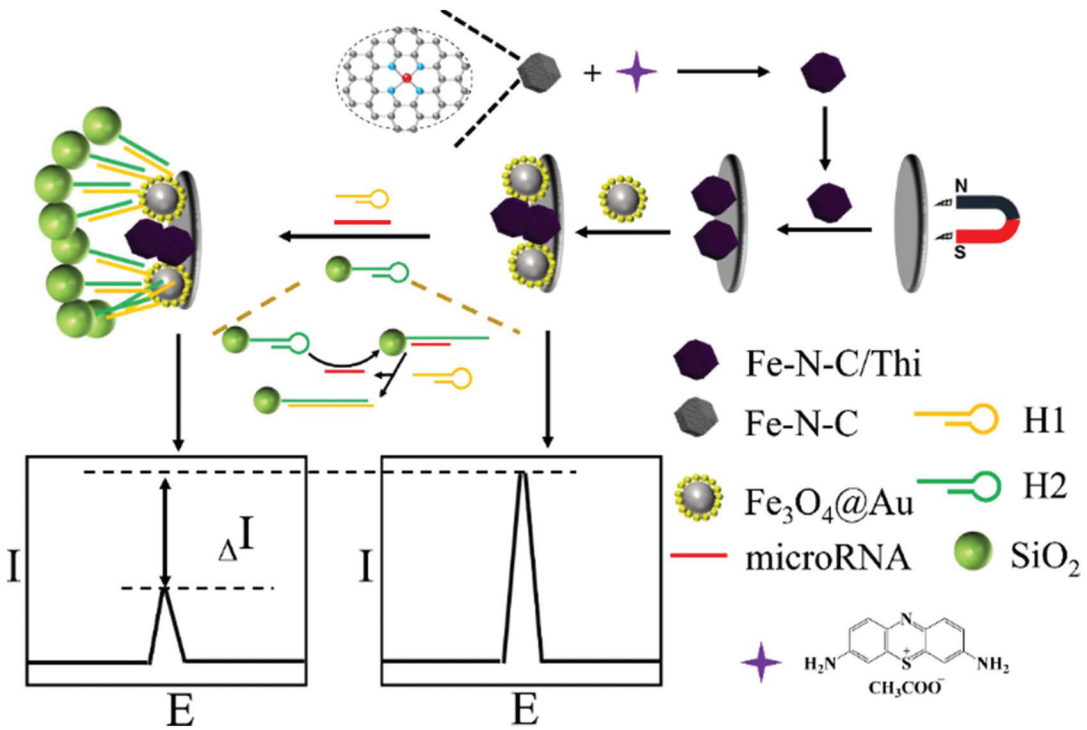


Scheme 1 Diagram of the proposed strategy for the detection of miRNA-21.

 

aminopropyl)carbodiimide (EDC), *N*-hydroxy succinimide (NHS), $HAuCl_4$, sodium citrate, tetraethyl orthosilicate (TEOS) and polyethyleneimine (PEI) were provided by Aladdin Reagent Co., Ltd. In this work, all oligonucleotides used were obtained from Sangon Biotech Co., Ltd, and the corresponding sequences are shown in Table S1.† Human serum samples (H4522) were purchased from Sigma-Aldrich. To inactivate the RNases and maintain the stability of the oligonucleotide, the micro tips, glassware and tubes were autoclaved.

### 2.2 Apparatus and measurements

A CHI660E electrochemical workstation (Shanghai Chenhua Instrument Corporation, China) was utilized to conduct all the electrochemical measurements. A three electrodes system was used in all electrochemical measurements. The three electrodes consist of a platinum wire electrode, a 3 mm diameter magnetic glass carbon electrode (MGCE), and a saturated calomel electrode (SCE). Cyclic voltammetry (CV), electrochemical impedance spectroscopy (EIS) and differential pulse voltammetry (DPV) were used in this work. SEM and TEM images were obtained using a Hitachi S-4800 and an FEI Tecnai G2 T20 microscope, respectively.

### 2.3 Preparation of the Fe–N–C electrocatalyst

A MOF derived Fe–N–C electrocatalyst was prepared according to Huang's method[40] with a few modifications. Firstly, ZIF-8 nanoparticles were prepared by mixing 4.2 g of $Zn(NO_3)_2{\cdot}6H_2O$ and 8.1 g of 2-methylimidazole in 480 ml of methanol and stirred vigorously for 20 h. The ZIF-8 precipitate was centrifuged and washed with methanol several times. Then, the collected ZIF-8 powder was dried at 65 °C for 12 h before use. Furthermore, 0.916 g of ZIF-8 was added to 200 mL of methanol and sonicated for 1 h. Subsequently, 64.8 mg of $FeCl_3$ was added to the above solution and the solution was kept stirring for 5 h at 25 °C. The $FeCl_3$@ZIF-8 precipitate was centrifuged and washed with methanol three times. After 12 h of dehydration at 70 °C, 0.93 g of $FeCl_3$@ZIF-8 was added to a KOH aqueous solution (100 mL, 15 mM) and stirred at 25 °C for 10 h. Next, the $Fe(OH)_3$@ZIF-8 precipitate was centrifuged, washed and dried. Then, the $Fe(OH)_3$@ZIF-8 powder was treated at 900 °C for 2 h under an Ar atmosphere. After that, the obtained product was added to 50 mL of $H_2SO_4$ (1 M) at 70 °C for 5 h to remove unstable species. Finally, the samples were washed and dried at 70 °C for 10 h, and the Fe–N–C electrocatalyst was obtained.

### 2.4 Synthesis of the Fe–N–C and thionine composite

To prepare a mixture of Fe–N–C and thionine, 2 mg of the Fe–N–C powder and 1 μM thionine was dispersed in 1 mL of $H_2O$ through ultrasonic oscillation for 4 h. Then, the Fe–N–C–thionine powder was centrifuged and washed with water. Then, the obtained Fe–N–C–thionine powder was dried at 65 °C for 10 h. Finally, the Fe–N–C–thionine powder was redispersed in water.

### 2.5 Synthesis of the $Fe_3O_4$@AuNPs

According to our previous work, $Fe_3O_4$ and AuNPs were synthesized respectively. The details of the procedure are displayed in the ESI.† $Fe_3O_4$@AuNPs were prepared through the self-assembly of positively charged $Fe_3O_4$ nanoparticles and negatively charged AuNPs. Briefly, 1 mL of PEI capped $Fe_3O_4$ nanoparticles (10 μM) and 1 mL of citrate capped AuNPs (10 mM) were mixed and sonicated for 1 h. After that, the formed $Fe_3O_4$@AuNPs were collected using an external magnet and redispersed in 1 mL of deionized water for use.

### 2.6 Synthesis of H2 modified $SiO_2$ nanospheres

Firstly, $SiO_2$ nanospheres were synthesized according to Stober's report. Briefly, 2.08 ml of TEOS was added to the mixture of 3 ml of deionized water and 90 ml of ethanol, and then 3.85 ml of ammonia water was mixed with the above solution with constant stirring for 20 h. $SiO_2$ nanospheres were collected through centrifugation and washed with deionized water three times. Then, the carboxyl group was grafted on the $SiO_2$ according to a previous report.[41] Briefly, 1 g of $SiO_2$ was dissolved in 200 ml of ethanol. Thereafter, 1 g of TESPSA was added to the above solution and the solution was kept stirring for 20 h. Then, the $SiO_2$–COOH nanospheres were collected through centrifugation and washed with water. After that, EDC (1 mL, 2 M) was utilized to activate the carboxyl group of the $SiO_2$–COOH (10 mg), and then NHS (0.2 mL, 1 M) and H2 (1 mL, 1 μM) were added to the above mixture. After stirring for 12 h, the H2–$SiO_2$ nanospheres were collected through centrifugation and washed with water.

### 2.7 Fabrication of the Fe–N–C–Thi/$Fe_3O_4$@AuNPs based electrochemical platform for the determination of miRNA-21

At first, bare MGCE was treated with 0.05 μm and 0.3 μm alumina–water slurries, and a mirror-like surface was obtained. Then, the MGCE was washed with water to remove residual particles. Furthermore, 10 μl of the Fe–N–C–thionine nanocomposite and 10 μl of $Fe_3O_4$@AuNPs were dropped onto the MGCE. After that, 10 μl of H1 treated with TCEP, 5 μl of miRNA-21 at various concentrations, and 10 μl of H2–$SiO_2$ were incubated at 37 °C for 2 h. Next, the incubation solution was dropped onto the above-modified electrode. Finally, the modified electrode was washed with PBS buffer to remove the non-specific adsorption. Then, the DPV response to the modified electrode was observed in PBS (pH = 7).

## 3 Results and discussion

### 3.1 Characterization of $SiO_2$ nanospheres, $Fe_3O_4$@AuNPs and the Fe–N–C catalyst

The morphology of the synthesized materials was observed by SEM and TEM. As shown in Fig. 1A and B, SEM reveals that the size of $SiO_2$ nanospheres was about 50–100 nm and the size of ZIF-8 was about 50–100 nm. Besides, the TEM image displayed the structures of $Fe_3O_4$@AuNPs (Fig. 1C) and Fe–N–C (Fig. 1D). The size of the AuNPs and $Fe_3O_4$ was about 20 nm

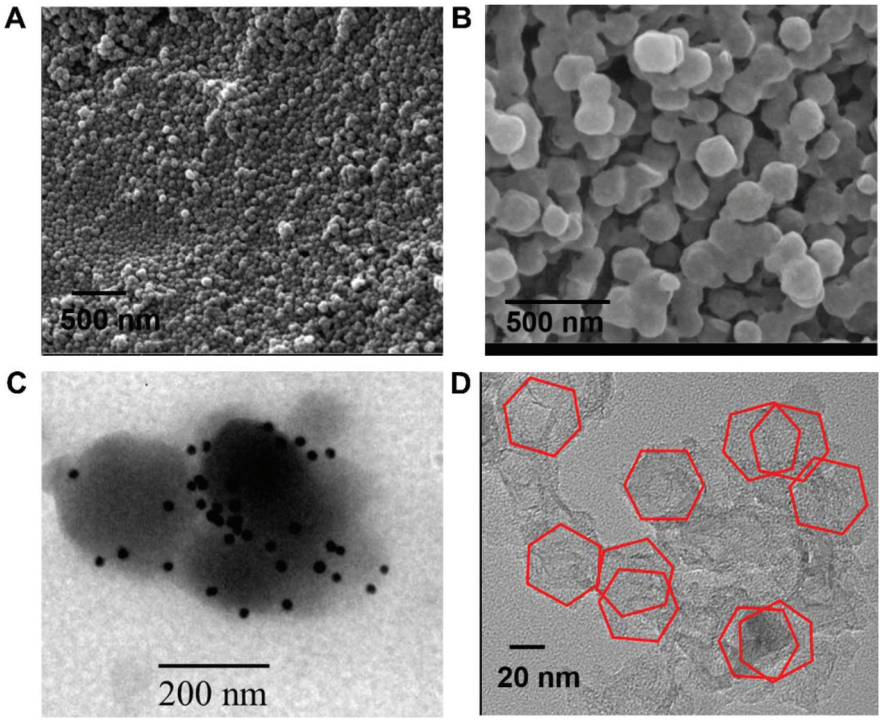


Fig. 1 SEM of (A) $SiO_2$ nanospheres and (B) ZIF-8 and TEM of (C) $Fe_3O_4$@AuNPs and (D) the Fe–N–C electrocatalyst.

and 170 nm, respectively. The shape of the Fe–N–C was similar to the previous report.[40] Furthermore, the corresponding elemental analysis results of $Fe_3O_4$@AuNPs and Fe–N–C are provided in Fig. S1.† These indicate that the $SiO_2$, $Fe_3O_4$@AuNPs and Fe–N–C were synthesized successfully.

### 3.2 The electroreduction performance of the Fe–N–C activity on thionine

At first, CV was carried out to explore the redox reaction of thionine on the Fe–N–C modified MGCE. As shown in Fig. 2A, different scan rates from 10 mV $s^{-1}$ to 100 mV $s^{-1}$ of thionine were used. A couple of redox peaks was observed for the potential range of −0.5 V to 0 V. Besides, as the sweep rates increased, all the redox peak currents became larger. In Fig. 2B, the maximum of cathodic peak current at −0.28 V *vs.* SCE was plotted as a function of the square root of sweep rate, which indicated that a linear relationship between the peak current and square root of sweep rate (square of the correlation coefficient, $R^2$ = 0.9932) was obtained. The cathodic peak current, for a diffusion-controlled process, is ideally linear in the square root of the sweep rate. Compared with the bare MGCE, the plot of $I_p$ *vs.* $V^{1/2}$ for the Fe–N–C modified MGCE displayed a steeper slope which verifies the catalytic ability of Fe–N–C in the electrochemical reduction of thionine.

According to the literature, $Fe_3O_4$ showed its narrow optimal pH range for the electrocatalytic reduction of thionine.[42] Therefore, the electrocatalytic activity of Fe–N–C was investigated in different solutions with various pH values. As shown in Fig. 2C, the Fe–N–C nanomaterials retained their electrocatalytic activity over a broad pH range of 1 to 7, which is superior to the previously reported biological enzyme and $Fe_3O_4$.[43] To further evaluate the electrocatalytic activity of Fe–N–C, different modified electrodes were compared and the results are shown in Fig. 2D. Since the optimal pH value of $Fe_3O_4$ for the electroreduction of thionine is 7,[43] the pH value for the following solution was determined to be 7. It was obvious that both Fe–N–C and the $Fe_3O_4$ modified MGCE showed their electrocatalytic reduction activity towards thionine for the great enhancement of the peak current. Besides, the peak potential shifted by −40 mV and −20 mV due to Fe–N–C and the $Fe_3O_4$ modified MGCE respectively. It could be that Fe–N–C and $Fe_3O_4$ accelerated the transfer of the electrons. This further proves that Fe–N–C and $Fe_3O_4$ co-efficiently catalyzed the electroreduction of thionine into leucothionine.

### 3.3 The stability of Fe–N–C in the electroreduction of thionine

CV was utilized to explore the stability of the Fe–N–C electrocatalyst in the electroreduction of thionine. As shown in Fig. S2A,† the Fe–N–C electrocatalyst preserved its electrocatalytic activity at a high level over multiple CV scans. The Fe–N–C modified MGCE was exposed to freshly prepared Thi (25 μM) during each scan. However, the corresponding peak currents of the electroreduction increased gradually after many cycles of the scan according to Fig. S2B.† It could be explained that the Fe–N–C catalyst was derived from ZIF-8 and the adsorption capacity[44] of the framework was retained. To further study the adsorption capacity of the Fe–N–C electroca-

 

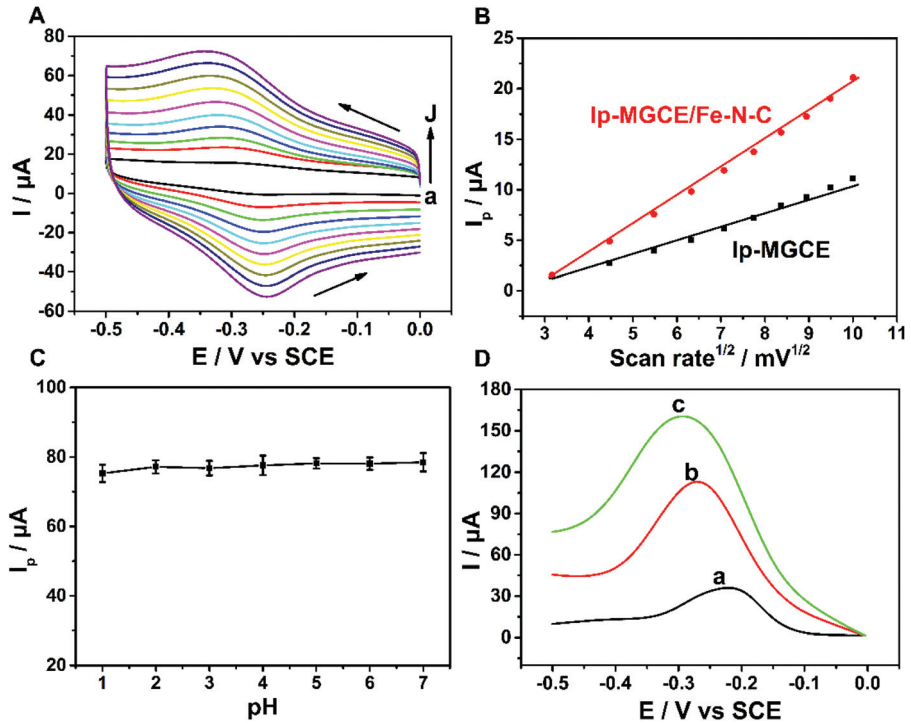


Fig. 2 (A) CV of different sweep rates (a) 10 mV $s^{-1}$, (b) 20 mV $s^{-1}$, (c) 30 mV $s^{-1}$, (d) 40 mV $s^{-1}$, (e) 50 mV $s^{-1}$, (f) 60 mV $s^{-1}$, (g) 70 mV $s^{-1}$, (h) 80 mV $s^{-1}$, (i) 90 mV $s^{-1}$ and (j) 100 mV $s^{-1}$ in the 25 μM thionine solution. (B) The linear relationship between the peak current and square root of the sweep rates. (Black line and red line represent bare MGCE and the Fe–N–C modified MGCE respectively.) (C) DPV responses to thionine (25 μM) with different pH values on MGCE/Fe–N–C. (D) DPV responses to thionine (25 μM, pH = 7) in different modified electrodes of (a) bare MGCE, (b) MGCE/Fe–N–C and (c) MGCE/Fe–N–C/$Fe_3O_4$.

talyst, the composite of Fe–N–C nanoparticles and thionine was modified on the MGCE, and their multiple cycles of CV conducted in PBS are shown in Fig. S3.† According to the results, CV responses to the composite of the Fe–N–C–thionine modified MGCE in PBS buffer displayed a more stable cyclic voltammogram and $I_p$. In the first 25 cycles, the $I_p$ has almost no change. After that, the $I_p$ was slightly decreased for the concentration diffusion between the electrode and the solution.

### 3.4 Electrochemical characterization of the fabricated electrode

The feasibility of the biosensor was studied by conducting CV and EIS.[45] Fig. 3A shows the cyclic voltammograms of the stepwise assembly interface in $[Fe(CN)_6]^{3-/4-}$. The reversible redox peaks of $[Fe(CN)_6]^{3-/4-}$ on the bare MGCE (curve a) were observed. After Fe–N–C–thionine/$Fe_3O_4$@AuNPs were modified onto the MGCE, the redox peak currents of the $[Fe(CN)_6]^{3-/4-}$ increased (curve b) the excellent conductivity of the composite Fe–N–C–thionine/$Fe_3O_4$@AuNPs and accelerated the transmission of electrons. The assembly of H1 (curve c) onto AuNPs leads to the decrease of the $I_p$ and the increase of the peak potential separation. It further reveals that H1 was assembled successfully by the Au–S bond. Along with the 1 pM of miRNA-21 matched with H1 (curve d), the $I_p$ only decreased slightly for its weak effect on the modified electrode with excellent conductivity. Then, the $I_p$ decreased after H2–$SiO_2$ further modified the electrode indicating the trigger of the catalytic hairpin assembly reaction among the H1, miRNA-21 and H2–$SiO_2$.

EIS results were consistent with cyclic voltammograms. From the Nyquist plot, the electron transfer resistance and solution resistance could be calculated.[46] In Fig. 3B, similar solution resistance could be observed. The Fe–N–C–thionine/$Fe_3O_4$@AuNPs modified electrode improved the conductivity, while the other modifications lead to more impedance. As a result, the construction of the modified electrode was successful.

### 3.5 Optimization of the measurement parameters

As shown in Fig. 3C, H1 with different concentrations ranging from 10 nM to 100 μM was modified onto the MGCE/Fe–N–C–thionine/$Fe_3O_4$@AuNPs. The rapid decrease in the $I_p$ from 10 nM to 10 μM could be observed. When the concentration of H1 is above 10 μM, there was almost no change in the $I_p$, which indicates that most of the AuNPs were attached with H1. Therefore, the optimal concentration of H1 used to incubate with miRNA-21 and H2–$SiO_2$ was determined to be 10 μM. Based on the scheme of our biosensor, the DPV signal should be changed as much as possible. According to our previous report, the catalytic hairpin assembly reaction was related to the incubation time.[47] Hence, different incubation times among the H1, miRNA-21, and H2–$SiO_2$ were used to optimize

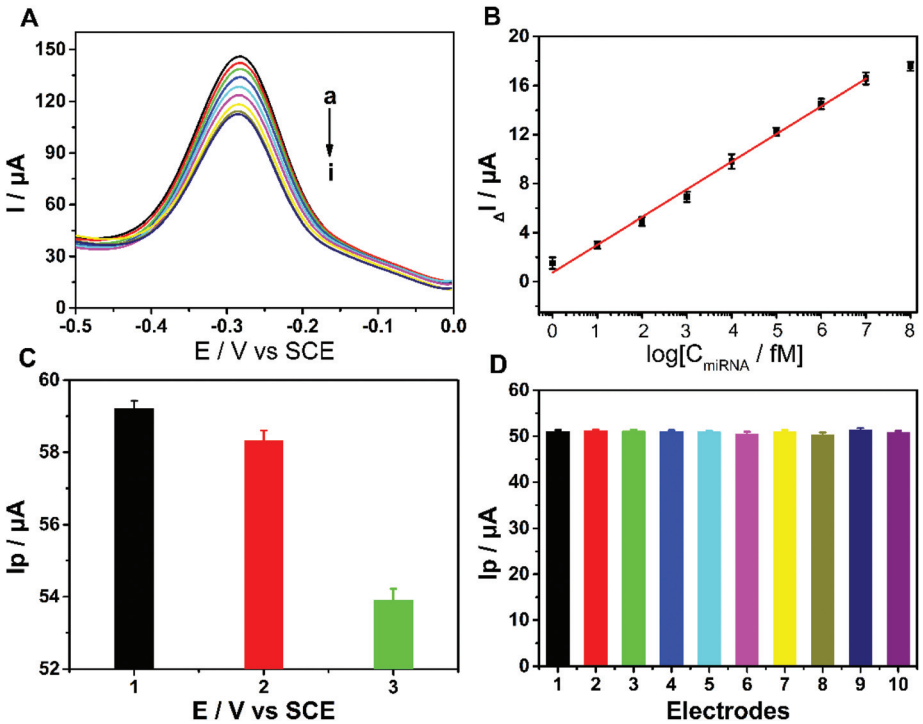


Fig. 3 (A) Cyclic voltammograms and (B) electrochemical impedance spectroscopy of the different modified electrodes: (a) bare MGCE, (b) MGCE/Fe–N–C–thionine/$Fe_3O_4$@AuNPs, (c) MGCE/Fe–N–C–thionine/$Fe_3O_4$@AuNPs–H1, (d) MGCE/Fe–N–C–thionine/$Fe_3O_4$@AuNPs–H1/miRNA-21 and (e) MGCE/Fe–N–C–thionine/$Fe_3O_4$@AuNPs–H1/miRNA-21/H2–$SiO_2$. (C) $I_p$ of DPV response to MGCE/Fe–N–C–thionine/$Fe_3O_4$@AuNPs modified with different concentrations of H1; (D) DPV response to MGCE/Fe–N–C–thionine/$Fe_3O_4$@AuNPs modified with H1, miRNA-21, and H2–$SiO_2$ at different incubation times from 0.5 h to 2.5 h.

the incubation time. The results shown in Fig. 3D are similar to those of our previous report,[47] and the optimal incubation time was 2 h.

### 3.6 Sensitivity, reproducibility and specificity of the constructed biosensor

Under the optimal measurement parameters, the analytical performance of the developed biosensor was explored. As displayed in Fig. 4A, the $I_p$ of the DPV became smaller as the concentration of the miRNA-21 increased from 0 to 100 nM. Correspondingly, the $\Delta I_p$ between the blank and the experiment also increased steadily. A linear relationship between the logarithm of miRNA-21 and $\Delta I_p$ in the range of 1 fM to 10 nM was obtained and is shown in Fig. 4B. The corresponding linear correlation equation is $\Delta I_p$ (μA) = 0.75 + 2.26 log$C$ ($R^2$ = 0.9976), where $C$ represents the concentration of miRNA-21 and $\Delta I_p$ represents the $I_p$ change ($\Delta I_p = Ip_{blank} - Ip_{experiment}$; $Ip_{blank}$ is the $I_p$ of the DPV for the electrode modified without miRNA-21 and $Ip_{experiment}$ is $I_p$ of the DPV for the electrode modified with different concentrations of miRNA-21). Besides, the limit of detection (LOD) was calculated to be 0.63 fM (signal/noise = 3). Table 1 lists some methods for the detection of miRNA-21 and other biomarkers. Compared with these methods, our LOD is low. However, this is the first study to utilize Fe–N–C in the electrochemical detection of miRNA-21.

To explore the specificity of the biosensor, the constructed biosensor was modified with other miRNAs instead of miRNA-21 such as single-base mismatched target and non-complementary miRNA. Fig. S4† shows the different results based on the non-complementary miRNA, single-base mismatched target and miRNA-21, and the corresponding $I_p$ values are compared in Fig. 4C. Obviously, the $I_p$ values of the non-complementary miRNA (a) and the single-base mismatched target (b) modified electrode were significantly higher than that of the target miRNA-21 (c). This could be explained as the target miRNA-21 can readily trigger a CHA reaction. In contrast, the single-base mismatched target and non-complementary miRNA could not trigger the CHA well because of its specificity. Also, the reproducibility of the biosensor was studied. Ten parallel experiments were conducted and the results are shown in Fig. 4D. We could observe that the peak current value among the ten parallel experiments only had a slight change, and the relative standard deviations (RSD) were 2.14%. Hence, the developed biosensor has excellent specificity and reproducibility.

### 3.7 Performance of the constructed biosensor in real samples

In order to study the applicability of the constructed biosensor, 100 fM, 1 pM, 100 pM, and 1 nM of miRNA-21 were prepared using human serum. Then, the 10-fold diluted samples were analyzed using the constructed biosensor. The

 

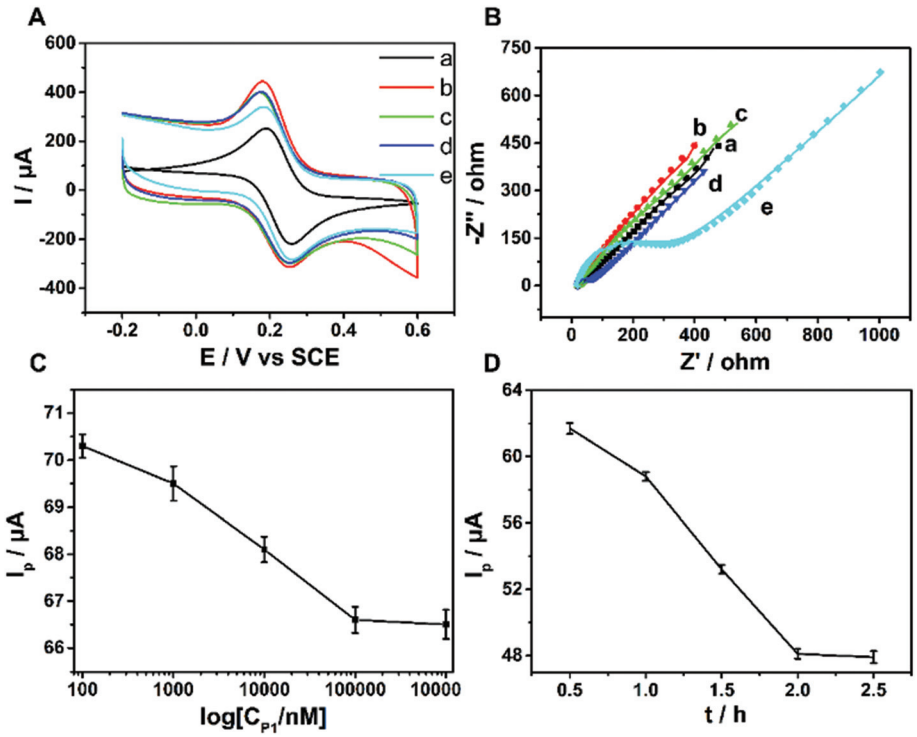


**Fig. 4** (A) DPV responses to the fabricated biosensor after incubation with different concentrations of miRNA-21 from (a) to (i): 0, 1 fM, 10 fM, 100 fM, 1 pM, 10 pM, 100 pM, 1 nM, 10 nM and 100 nM; (B) calibration curve of peak current *vs.* different miRNA-21 concentrations. Error bars = RSD ($n$ = 5); (C) DPV responses to the developed biosensor in specificity for the (a) 10 pM of non-complementary miRNA, (b) 10 pM of single-base mismatched target and (c) 1 pM of miRNA-21; (D) DPV responses to the independently fabricated ten biosensors and the concentration of target miRNA-21 is 10 pM.

**Table 1** Comparison of different biosensors for the detection of nucleic acids

| Detection method | Target | Signal amplification strategy | LOD | Ref. |
|---|---|---|---|---|
| Fluorescence | miRNA-21 | SDR | 0.13 nM | 48 |
| SWV | miRNA-133 | Ratiometric | 0.3 pM | 49 |
| DPV | CEA | SDR and MB@DNA/MOFs | 16 fg | 50 |
| SWV | miRNA-155 | Nanozyme catalytic reaction | 0.13 fM | 51 |
| DPV | miRNA-21 | $Fe[(CN)_6]^{3-}$ | 10 fM | 52 |
| Fluorescence | miRNA-122 | CHA reaction | 72 pM | 53 |
| DPV | miRNA-155 | Nanozyme and strand displacement reaction | 0.35 fM | 54 |
| DPV | miRNA-21 | Fe–N–C–thionine/$Fe_3O_4$ electrocatalyst and CHA reaction | 0.63 fM | This work |

results (Table S2†) showed that the distribution of the recovery was between 96.97% and 102.33%, and the RSDs were below 4.36%.

## 4 Conclusion

In summary, a thionine functionalized MOF derived Fe–N–C nanocomposite was employed as a substrate for the construction of a novel label-free electrochemical platform for the detection of miRNA-21. Furthermore, the highly efficient electrocatalytic reduction activity of Fe–N–C towards thionine was explored and verified. Besides, the Fe–N–C electrocatalyst retains its activity in a wide pH range. The Fe–N–C–thionine/$Fe_3O_4$@AuNPs nanocomposite combined the electrocatalysis with signal amplification properties and exhibited significantly robust electrocatalytic activity. The CHA reaction further improved the sensitivity of the constructed biosensor. Also, this electrochemical strategy may be readily utilized for the electrochemical sensing of other types of tumor biomarkers by functionalization of the nanohybrids with other capture probes like antibodies or aptamers, which indicates its great potential in the early-stage diagnosis of tumors.

## Conflicts of interest

There are no conflicts to declare.

## Acknowledgements

This investigation was financially supported by the National Natural Science Foundation of China (No. 81571812) and A Project Funded by the Priority Academic Program Development of Jiangsu Higher Education Institutions (1107047002).

## Notes and references

1 A. Qureshi and J. H. Niazi, *Analyst*, 2020, **145**, 7825–7848.
2 X. Ma, H. Xu, K. Qian, M. Kandawa-Schulz, W. Miao and Y. Wang, *Talanta*, 2020, **208**, 120441.
3 A. Kumar, B. Purohit, P. K. Maurya, L. M. Pandey and P. Chandra, *Electroanalysis*, 2019, **31**, 1615–1629.
4 S.-H. Wu, X.-B. Huang, Y. Tang, L.-M. Ma, Y. Liu and J.-J. Sun, *Anal. Chim. Acta*, 2020, **1096**, 44–52.
5 Y. Lin, L. Hu, L. Yin and L. Guo, *Sens. Actuators, B*, 2015, **210**, 513–518.
6 F. N. Muya, P. G. L. Baker and E. I. Iwuoha, *Electrocatalysis*, 2020, **11**, 374–382.
7 Z. Liu, H. Tan, J. Xin, J. Duan, X. Su, P. Hao, J. Xie, J. Zhan, J. Zhang, J.-J. Wang and H. Liu, *ACS Appl. Mater. Interfaces*, 2018, **10**, 3699–3706.
8 T.-N. Pham-Truong, O. Mebarki, C. Ranjan, H. Randriamahazaka and J. Ghilane, *ACS Appl. Mater. Interfaces*, 2019, **11**, 38265–38275.
9 Y. Liu, S. Chen, X. Quan and H. Yu, *J. Am. Chem. Soc.*, 2015, **137**, 11631–11636.
10 M. Zhang, C. Choi, R. Huo, G. H. Gu, S. Hong, C. Yan, S. Xu, A. W. Robertson, J. Qiu, Y. Jung and Z. Sun, *Nano Energy*, 2020, **68**, 104323.
11 B. Yu, Y. Chen, Z. Wang, D. Chen, X. Wang, W. Zhang, J. He and W. He, *J. Power Sources*, 2020, **447**, 227364.
12 H. Li, L. Li, R.-B. Lin, W. Zhou, Z. Zhang, S. Xiang and B. Chen, *EnergyChem*, 2019, **1**, 100006.
13 X. Li, S. Zheng, L. Jin, Y. Li, P. Geng, H. Xue, H. Pang and Q. Xu, *Adv. Energy Mater.*, 2018, **8**, 1800716.
14 K. Suresh and A. J. Matzger, *Angew. Chem., Int. Ed.*, 2019, **58**, 16790–16794.
15 B. E. Souza, L. Donà, K. Titov, P. Bruzzese, Z. Zeng, Y. Zhang, A. S. Babal, A. F. Möslein, M. D. Frogley, M. Wolna, G. Cinque, B. Civalleri and J.-C. Tan, *ACS Appl. Mater. Interfaces*, 2020, **12**, 5147–5156.
16 L. C. D. Batista, T. I. S. Santos, J. E. L. Santos, D. R. da Silva and C. A. Martínez-Huitle, *Electroanalysis*, 2021, **33**, 57.
17 J.-O. Kim, J. Y. Kim, J.-C. Lee, S. Park, H. R. Moon and D.-P. Kim, *ACS Appl. Mater. Interfaces*, 2019, **11**, 4385–4392.
18 Y.-S. Chang, J.-H. Li, Y.-C. Chen, W. H. Ho, Y.-D. Song and C.-W. Kung, *Electrochim. Acta*, 2020, **347**, 136276.
19 U. Ryu, S. Jee, P. C. Rao, J. Shin, C. Ko, M. Yoon, K. S. Park and K. M. Choi, *Coord. Chem. Rev.*, 2021, **426**, 213544.
20 X. Zhang, G. Li, D. Wu, X. Li, N. Hu, J. Chen, G. Chen and Y. Wu, *Biosens. Bioelectron.*, 2019, **137**, 178–198.
21 J. Mehta, N. Bhardwaj, S. K. Bhardwaj, K.-H. Kim and A. Deep, *Coord. Chem. Rev.*, 2016, **322**, 30–40.
22 A. Karmakar, P. Samanta, A. V. Desai and S. K. Ghosh, *Acc. Chem. Res.*, 2017, **50**, 2457–2469.
23 R. Banerjee, A. Phan, B. Wang, C. Knobler, H. Furukawa, M. Keeffe and O. M. Yaghi, *Science*, 2008, **319**, 939.
24 M. Lu, Y. Deng, Y. Li, T. Li, J. Xu, S.-W. Chen and J. Wang, *Anal. Chim. Acta*, 2020, **1110**, 35–43.
25 Y. Wang, M. Zhao, C. Hou, X. Yang, Z. Li, Q. Meng and C. Liang, *J. Taiwan Inst. Chem. Eng.*, 2019, **102**, 312–320.
26 X. Niu, X. Li, Z. Lyu, J. Pan, S. Ding, X. Ruan, W. Zhu, D. Du and Y. Lin, *Chem. Commun.*, 2020, **56**, 11338–11353.
27 Z. Sun, L. Wang, S. Wu, Y. Pan, Y. Dong, S. Zhu, J. Yang, Y. Yin and G. Li, *Anal. Chem.*, 2020, **92**, 3819–3826.
28 D. Sheberla, J. C. Bachman, J. S. Elias, C.-J. Sun, Y. Shao-Horn and M. Dincă, *Nat. Mater.*, 2017, **16**, 220–224.
29 Y. Jiang, I. Oh, S. H. Joo, Y.-S. Seo, S. H. Lee, W. K. Seong, Y. J. Kim, J. Hwang, S. K. Kwak, J.-W. Yoo and R. S. Ruoff, *J. Am. Chem. Soc.*, 2021, **142**(43), 18346–18354.
30 C. Singh, I. Liberman, R. Shimoni, R. Ifraemov and I. Hod, *J. Phys. Chem. Lett.*, 2019, **10**, 3630–3636.
31 J. Sun, L. Sun, S. Bai, H. Fu, J. Guo, Y. Feng, R. Luo, D. Li and A. Chen, *Sens. Actuators, B*, 2019, **285**, 291–301.
32 M. Wang, N. Zhang, Y. Feng, Z. Hu, Q. Shao and X. Huang, *Angew. Chem., Int. Ed.*, 2020, **59**, 14373–14377.
33 S. A. M. Rizvi, N. Iqbal, M. D. Haider, T. Noor, R. Anwar and S. Hanif, *Catal. Lett.*, 2020, **150**, 1397–1407.
34 Ö. Akarçay, S. F. Kurtoğlu and A. Uzun, *Int. J. Hydrogen Energy*, 2020, **45**, 28664–28681.
35 L. Wang, J.-W. Zhang, C. Li, J.-L. Sun, G.-M. Wang and Y.-Z. Chen, *Dalton Trans.*, 2020, **49**, 10567–10573.
36 H. Zhang, J. Li, S. Xi, Y. Du, X. Hai, J. Wang, H. Xu, G. Wu, J. Zhang, J. Lu and J. Wang, *Angew. Chem., Int. Ed.*, 2019, **58**, 14871–14876.
37 M. Sharifi, M. R. Avadi, F. Attar, F. Dashtestani, H. Ghorchian, S. M. Rezayat, A. A. Saboury and M. Falahati, *Biosens. Bioelectron.*, 2019, **126**, 773–784.
38 Y. Chen, N. Wu, L. Liu, H. Dong and C. Wu, *Clin. Biochem.*, 2019, **71**, 52–57.
39 P. Yadav, M. Mirza, K. Nandi, S. K. Jain, R. C. M. Kaza, N. Khurana, P. C. Ray and A. Saxena, *Tumor Biol.*, 2016, **37**, 15275–15282.
40 J.-W. Huang, Q.-Q. Cheng, Y.-C. Huang, H.-C. Yao, H.-B. Zhu and H. Yang, *ACS Appl. Energy Mater.*, 2019, **2**, 3194–3203.
41 A. I. Barabanova, T. A. Pryakhina, E. S. Afanas'ev, B. G. Zavin, Y. S. Vygodskii, A. A. Askadskii, O. E. Philippova and A. R. Khokhlov, *Appl. Surf. Sci.*, 2012, **258**, 3168–3172.
42 C. Ruan, F. Yang, C. Lei and J. Deng, *Anal. Chem.*, 1998, **70**, 1721–1725.
43 T. Zheng, Q. Zhang, S. Feng, J.-J. Zhu, Q. Wang and H. Wang, *J. Am. Chem. Soc.*, 2014, **136**, 2288–2291.
44 S. Tanaka, K. Fujita, Y. Miyake, M. Miyamoto, Y. Hasegawa, T. Makino, S. Van der Perre, J. Cousin Saint Remi, T. Van

 

Assche, G. V. Baron and J. F. M. Denayer, *J. Phys. Chem. C*, 2015, **119**, 28430–28439.
45 E. Xiong, X. Zhang, Y. Liu, J. Zhou, P. Yu, X. Li and J. Chen, *Anal. Chem.*, 2015, **87**, 7291–7296.
46 L. Zhang, X. Xiao, Y. Xu, D. Chen, J. Chen, Y. Ma, Z. Dai and X. Zou, *Biosens. Bioelectron.*, 2018, **100**, 184–191.
47 X. Ma, K. Qian, O. Ejeromedoghene, M. Kandawa-Schulz and Y. Wang, *Electrochim. Acta*, 2020, **362**, 137168.
48 X.-J. Kong, X. Ji, T. He, L.-H. Xie, Y.-Z. Zhang, H. Lv, C. Ding and J.-R. Li, *ACS Appl. Mater. Interfaces*, 2020, **12**, 35375–35384.
49 Y. Sun, H. Jin, X. Jiang and R. Gui, *Sens. Actuators, B*, 2020, **309**, 127777.
50 T. Bao, R. Fu, W. Wen, X. Zhang and S. Wang, *ACS Appl. Mater. Interfaces*, 2020, **12**, 2087–2094.
51 Z. Liang, D. Ou, D. Sun, Y. Tong, H. Luo and Z. Chen, *Biosens. Bioelectron.*, 2019, **146**, 111744.
52 S. Shin Low, Y. Pan, D. Ji, Y. Li, Y. Lu, Y. He, Q. Chen and Q. Liu, *Sens. Actuators, B*, 2020, **308**, 127718.
53 Y. Liu, T. Shen, J. Li, H. Gong, C. Chen, X. Chen and C. Cai, *ACS Sens.*, 2017, **2**, 1430–1434.
54 H. Wang, Y. Jian, Q. Kong, H. Liu, F. Lan, L. Liang, S. Ge and J. Yu, *Sens. Actuators, B*, 2018, **257**, 561–569.